Earth and Planetary Science Letters 279 (2009) 11–19

Contents lists available at ScienceDirect

Earth and Planetary Science Letters

journal homepage: www.elsevier.com/locate/epsl

# Structure and elasticity of serpentine at high-pressure

Mainak Mookherjee [a,*], Lars Stixrude [b]

[a] Bayerisches Geoinstitut, University of Bayreuth, D-95444 Bayreuth, Germany
[b] Department of Earth Sciences, University College London, London, WC1E 6T, UK

ARTICLE INFO

*Article history:*
Received 10 September 2008
Received in revised form 8 December 2008
Accepted 9 December 2008
Available online 29 January 2009

Editor: R.D. van der Hilst

*Keywords:*
subduction
fore-arc mantle
serpentine
elasticity
amorphization

ABSTRACT

Serpentines occur in the subduction zone settings, both along the slab and within the mantle wedge, they are candidates for transporting water in to the deep earth. Their presence is manifested by serpentine mud volcanoes, high electrical conductivities, magnetic and seismic anomalies.
Using theoretical methods, we predict a pressure induced structural transformations in serpentine. The transformations are related to the behavior of the silicate framework and misfit between octahedral and tetrahedral layers. As the structure is compressed, the octahedral layer and tetrahedral layers are compressed at different rates. At 7 GPa, the misfit between the layers vanishes. This causes non-linear pressure dependence of tetrahedral rotational angle. This is also manifested by the onset of anomalous pressure dependence of the elastic constants $c_{11}$, $c_{33}$, $c_{12}$, $c_{13}$. Beyond 7 GPa, the misfit between the layers grows again reaching extremum at 22 GPa. This is also manifested by discontinuity in average Si–O bond length, volume of tetrahedron and re-orientation of hydroxyl vector. The symmetry of the crystal-structure however, remains unaffected. Evidence of pressure-induced hydrogen bonding is absent in serpentine, as evident from reduction of O–H bond length upon compression. Results of compression for the low-pressure regime ($P<7$ GPa) is well represented by a fourth order Birch–Murnaghan finite strain expression with $K_0=79$ GPa, $K_0'=12$ and $K_0''=-2$, where $K$ is the bulk modulus, prime indicates pressure derivatives, and O refers to zero pressure. Our best estimates of $K_0$, $K_0'$ and the Grüneisen parameter, $\gamma$ at 300 K and zero pressure based on our results are: 61 GPa, 17, and 0.77, respectively. At low pressures, serpentine structure is anisotropic with $c_{11}\sim 2.4\times c_{33}$. The pressure derivative of elastic constants ($\partial c_{ij}/\partial P$) are such, that around 22 GPa $c_{11}\sim c_{33}$. An elastic instability ($c_{66}<0$) at somewhat higher pressures (>50 GPa) is also noted. The elastic constant tensor reveals large acoustic anisotropy (41% in $V_P$) and seismic wave velocities that are significantly higher than those inferred from experiments on serpentinites.


## 1. Introduction

Phyllosilicates such as serpentine occurring in fine-grained chondrites are thought of as primary contributor towards the earth's total water inventory during its formation (Tyburczy et al., 1991; Ciesla et al., 2003). In the present day earth, serpentine occurs as an alteration product of peridotites in the oceanic lithosphere. On subduction, serpentine dehydrates between 150 and 250 km depth (5–8 GPa), releasing 13 wt.% water, a phenomonen that has been linked to intermediate earthquakes occurring along subduction zone (Dobson et al., 2002; Obara, 2002). The water released is thought to migrate upward into the hotter overlying mantle causing partial melting and in part controlling the location of the volcanic arc. In cold slabs, serpentine may persist metastably to greater depths where its amorphization has also been suggested as a source of deep seismicity (Meade and Jeanloz, 1991), although the extent of metastability may be less than previously thought (Irifune et al., 1996).

The fore-arcs of non-accretionary convergent margin such as Mariana is pervasively faulted. They contain numerous mud-volcanoes composed of unconsolidated flows of serpentine muds containing clasts of serpentinized mantle peridotites (Fryer et al., 1999). High-velocity crustal material overlies lower-velocity mantle material causing a discontinuity, referred to as an “inverted Moho” (Bostock et al., 2002). This is attributed to the presence of serpentine in the fore-arc mantle, possibly associated with metasomatism from subduction-related fluid release. Serpentine along with other alteration products such as brucite and talc in the fore-arc mantle exhibits stable sliding behaviour at plate velocities and could inhibit brittle behavior (Reinen, 2000). The weak rheology of the hydrous phases, may isolate the hydrated fore-arc region from the mantle-wedge corner flow system (Hilairet et al., 2007).

Despite the importance of serpentine for our understanding of upper mantle structure, dynamics, and melting behavior, little is known of its atomic structure or elasticity at high pressure beyond the equation of state (Mellini and Zanazzi, 1989; Tyburczy et al., 1991; Hilairet et al., 2006a,b), the Raman spectrum (Auzende et al., 2004), and the whole-rock P- and S-wave velocities of serpentinites up to 1 GPa (Christensen, 2004). In particular the nature of hydrogen bonding in serpentine at high pressure, which may lend insight into

* Corresponding author. Tel.: +49 921 55 3746; fax: +49 921 55 3769.
*E-mail address:* mainak.mookherjee@uni-bayreuth.de (M. Mookherjee).

0012-821X/$ – see front matter © 2008 Elsevier B.V. All rights reserved.
doi:10.1016/j.epsl.2008.12.018

stable and metastable dehydration is still poorly understood. Understanding of the elasticity of serpentine is essential for related seismological observations to the degree of serpentinization.

In the present study we explore the high-pressure behavior of serpentine. We find previously unsuspected pressure-induced structural rearrangements, driven by changes in hydrogen bonding, that we are able to relate to anomalies in elastic properties within the serpentine stability field.

## 2. Methods

Density functional theory (Kohn and Sham, 1965) has proven to be a powerful tool for studying the structure and thermodynamics of Earth materials at high pressure (Stixrude et al., 1998). While the theory is exact, the exact form of exchange-correlation is unknown and must be approximated. We investigate two widely used approximations: the local density (LDA) and generalized gradient (GGA) approximations (Lundqvist and March, 1987; Perdew et al., 1996). It is argued that the core electrons participate little in bonding and structural changes over the ranges of interest. Hence a further approximation known as the pseudopotential approximations (Heine, 1970) is also made. We use ultra-soft Vanderbilt (Vanderbilt, 1990; Kresse et al., 1992) pseudopotentials which limit the size of the plane wave basis set that is required to accurately represent the charge density and potential. Static calculations are performed with the Vienna ab-initio simulation package (VASP) (Kresse and Hafner, 1993; Kresse and Furthmüller, 1996a,b). Calculated forces and stresses are used to perform complete structural relaxation at constant volume. A conjugate gradient scheme (Wentzcovitch, 1991) systematically modifies the structure, conserving the space group symmetry (Wentzcovitch et al., 1993), until the net forces and deviatoric stresses fall below a tolerance threshold. To determine the elastic constants we first determined the equilibrium structure at each pressure. The unit-cell of the relaxed structure was then subjected to a chosen strain and re-optimized. We applied positive and negative strains of magnitude 1%, in order to accurately determine the stresses in the appropriate limit of zero strain. The strained lattice $a'$ is related to the unstrained lattice $a$ by $a'=(I+\varepsilon)a$, where I is the identity matrix. Four distinct strain tensors were applied: $\varepsilon_{11}$; $\varepsilon_{21}=\varepsilon_{12}$; $\varepsilon_{31}=\varepsilon_{13}$; $\varepsilon_{33}$ on a hexagonal lattice. The elastic constants determined are the stress-strain coefficients, which are those that govern elastic wave propagation, and stability criteria at general (finite) pressure (Wallace, 1972). The detail of the method adopted is outlined in Karki et al. (2001).

We focus on the lizardite-1T polytype $Mg_3Si_2O_5(OH)_4$, which may be considered the minimal ($m=1$) polysome of antigorite (Grobéty, 2003), the stable phase at elevated pressure and temperature. The lizardite-1T crystal structure has trigonal $P3_1m$ space-group symmetry (Rucklidge and Zussman, 1965; Mellini and Zanazzi, 1989). All computations are performed in the primitive unit cell (18 atoms, i.e., one formula unit). We used an energy cutoff $E_{cut}=600$ eV, and a Monkhurst-Pack (Monckhurst and Pack, 1976) 2×2×2 $k$-point mesh, yielding 3 $k$ points in the irreducible wedge of the Brillouin zone. A series of convergence test demonstrated that these computational parameters yield pressures and total energies that are converged within 0.01 GPa and 10 meV respectively. Previous studies have shown that density functional theory captures the relevant physics of hydrous minerals with varying bond strengths from strong hydroxyl to weak interlayer forces (Stixrude, 2002; Stixrude and Peacor, 2002; Mookherjee and Stixrude, 2006).

## 3. Results

### 3.1. Equation of state

We find that the Birch–Murnaghan eqution of state (Birch, 1978) fails to describe the compression behavior of serpentine over the entire range of our calculations. We therefore analyze the pressure–volume relationship in three distinct regions, a low-pressure region defined by unit-cell volumes 210 to 160 Å$^3$ ($P<7$ GPa), an intermediate pressure region with the unit-cell volume between 160 to 135 Å$^3$ (7 GPa$<P<$22 GPa and a high pressure region defined by volumes smaller than 135 Å$^3$ ($P>22$ GPa) (Fig. 1a). These regions are defined by changes in structure and bonding as described below.

The static zero pressure volume within LDA is 4.3% smaller, and that within GGA is 4.5% larger than that of the room temperature experimental value (Table 1). The static zero pressure value of the bulk modulus within LDA is 40% larger, and that within GGA is 28% smaller than that found in room temperature experiments. These differences are similar to those found in talc (Stixrude, 2002) and are attributed to the influence of phonon excitation, and the approximations to the exchange-correlation functional. Since our calculations are static, we expect phonon excitation to increase the zero pressure volume and to decrease the zero pressure bulk modulus relative to our theoretical values, leading to improved agreement between LDA and experiment, and an increase in the discrepancy between GGA and experiment. Because LDA shows substantially better agreement with experiment, further discussion focuses on LDA.

We estimate the influence of phonon excitation, following our previous work (Stixrude, 2002; Stixrude and Lithgow-Bertelloni, 2005), using a Debye–Grüneisen model

$$P(V,T)=P_{\mathrm{LDA}}(V)+\frac{\gamma}{V}[E_Z(V)+E_{TH}(V,T)] \quad (1)$$

$$K(V,T)=K_{\mathrm{LDA}}(V)+\frac{\gamma}{V}(\gamma+1-q)[E_Z(V)+E_{TH}(V,T)]-\frac{\gamma^2}{V}TC_V(V,T) \quad (2)$$

where $V$ is volume, and $C_V$, the isochoric heat capacity, and $E_Z$ and $E_{TH}$ the zero-point and thermal energies, respectively, are computed within the Debye model, which depends on the Debye temperature $\theta$, the Grüneisen parameter, $\gamma=V\alpha K_T/C_V$, where $\alpha$ is the thermal expansivity, $K_T$ is the isothermal bulk modulus, and the logarithmic volume derivative of $\gamma$, $q$. We choose values of these parameters on the basis of experiment. Combined with our static equation of state (LDA), we find that the following values: $\theta_0=830$ K (Stixrude, 2002), $\gamma_0=0.68$, $q=1$ (assumed) reproduce laboratory measurements of the thermal expansivity at ambient conditions ($\alpha=3.28\times10^{-5}$ K$^{-1}$, Gregorkiewitz et al., 1996), and the heat capacity at 900 K ($C_P=410.5$ J mol$^{-1}$ K$^{-1}$, Robie and Hemmingway, 1995). Applying corrections for phonon excitation in this way yields values at 300 K in good agreement with experiment: $V_0=104.5$ cm$^3$ mol$^{-1}$, $K_0=60.3$ GPa, which are smaller than experimental values by 3% and 13% respectively. Part of the remaining discrepancy in the bulk modulus may be due to experimental uncertainty due to the trade-off between $K_0$ and $K_0'$ when fitting equation of state data: the higher experimental value of $K_0$ is complemented by a lower value of $K_0'$ as compared with our results.

The linear compressibilities were analyzed using third-order finite strain theory (Birch, 1978; Meade and Jeanloz, 1990). The linear compressibility exhibits anisotropy, the in-plane stiffness ([100] direction) being almost 3 times larger than the interlayer stiffness ([001] direction) with $K_a=381$ GPa and $K_c=137$ GPa. The linear stiffnesses are in excellent agreement with Hilairet et al. (2006b) who report $K_a=370$ GPa and $K_c=103$ GPa respectively. This is significantly better in comparison to the atomistic simulations (Auzende et al., 2006) which predict $K_a=434$ GPa and $K_c=48$ GPa respectively. The $c/a$ ratio decreases rapidly from 1.6 to 1.3 upon initial compression, and then flattens out upon further compression, in excellent agreement with experiment. The trend of the $c/a$ ratio exhibits discontinuities at 7 and 22 GPa related to structural changes at the boundaries between low, medium, and high pressure regimes (Fig. 1b).

We predict a spinodal instability in serpentine upon expansion by 3.7% (at −3 GPa) from the experimental ambient volume. A similar feature has been noted in talc (Stixrude, 2002). The spinodal is

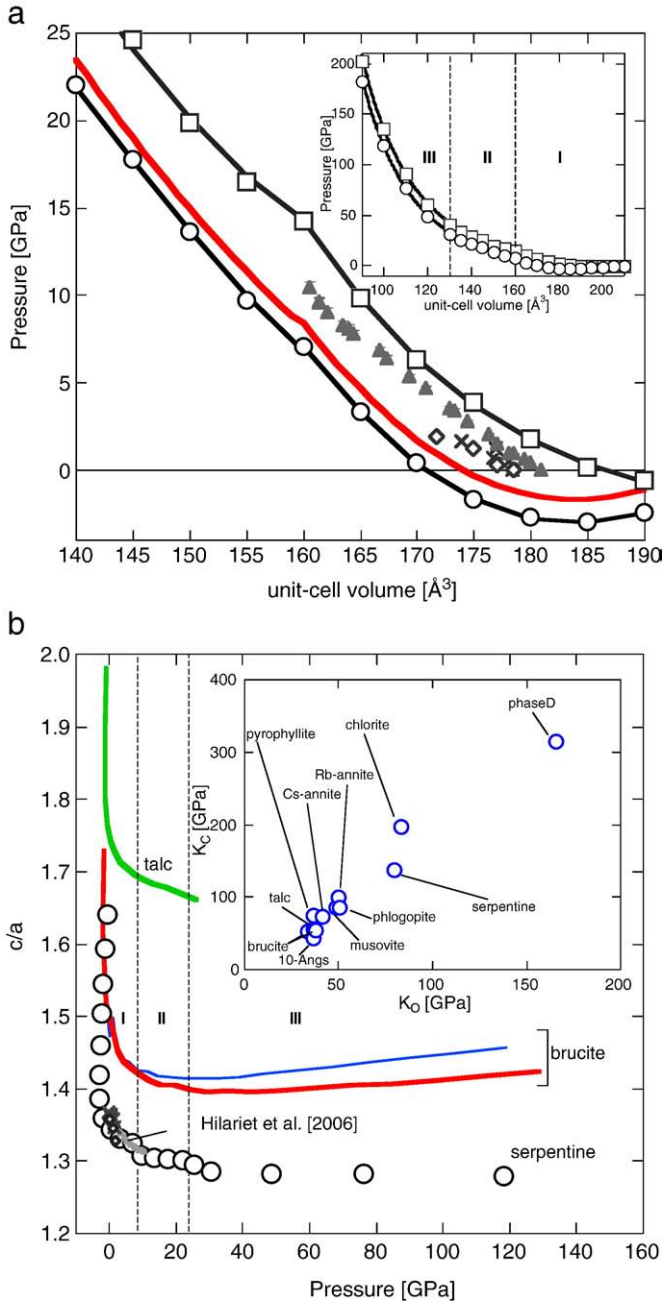


**Fig. 1.** a) Equation of state of serpentine: Open circles, LDA theory; black open squares, GGA theory; black solid line, finite strain fit to LDA results for $V=210$ to 160 Å$^3$ and $V=160$ to 140 Å$^3$; black solid line, finite strain fit to GGA results; red line finite strain fit for LDA pressures with zero point and thermal corrections to 300 K; grey filled triangle; experimental (Hilariet et al., 2006); black open rhombs and crosses, experimental (Mellini and Zanazzi, 1989). Inset shows the entire P–V data for LDA and GGA, three distinct regions labeled I ($V=160$ Å$^3$ and 7 GPa), II ($V=140$ Å$^3$ and 22 GPa), and III whose boundaries corresponds to structural changes that occur in lizardite; b) Pressure dependence of $c/a$ parameter: Open circles represents lizardite LDA theory; red and blue lines represent brucite GGA theory with proton in 2d and 6i crystallographic positions respectively (Mookherjee and Stixrude, 2006); green line represents talc LDA theory (Stixrude, 2002); grey triangles, rhombs and circles represent experimental results (Mellini and Zanazzi, 1989; Hilairet et al., 2006b) on lizardite. Note the discontinuity of $c/a$ at 7 and 22 GPa, indicating reorganization of the structure. Inset shows a plot of bulk modulus ($K_0$) vs. linear moduli ($K_c$) for a series of layered hydrous silicate minerals, they show a positive correlation, possibly hinting towards the fact that compressibility in layer silicates are often dictated by compressibility along their weakest direction. Data are from various sources: brucite, Xia et al. (1998) and Jiang et al. (2006); talc, Stixrude (2002); pyrophyllite and chlorite, Pawley et al. (2002); 10 A, Comodi et al. (2006); Cs- and Rb-annite, Comodi et al. (1999); Muscovite, Comodi and Zanazzi (1995); phlogopite, Hazen and Finger (1978) and phase D, Frost and Fei (1999).

characterized by vanishing bulk modulus ($K\approx0$) i.e. where pressure is minimum, further expansion of the volume will not result in further reduction in the pressure. Hence, at −3 GPa, a defect free homogeneous serpentine is mechanically unstable and is expected to fragment. This is the theoretical prediction of hydrostatic tensile strength and is distinct from strength under uniaxial tension, which could be substantially lower owing to the anisotropic nature of serpentine.

### 3.2. Structure and behaviour of proton

The serpentine structure consists of alternating layers of tetrahedral and octahedral sheets (1:1 T–O layers, Rucklidge and Zussman, 1965). We characterize the structure with the tetrahedral and octahedral bond lengths; octahedral flattening angle $\psi=\cos^{-1}[t_{oct}/(2<M-O>)]$ where $t_{oct}$ is the octahedral thickness (calculated from the difference in $z$ coordinate of the oxygen atoms of octahedron) and $<M-O>$ is the average octahedral bond length; tetrahedral flattening angle; tetrahedral rotation angle, $\alpha=\sum_{i=1}^{6}|120°-\phi_i|/12$ where $\phi_i$ is the angle between basal edges of neighboring tetrahedra articulated in a ring and the misfit between the tetrahedral layer and octahedral layer depicted by the oxygen lattice corrugation, $\Delta z=[zO_{max}-zO_{min}]\times c$, where $z_O$ is the $z$ crystallographic coordinate of the basal O atom. The crystal structure contains two distinct proton sites: the H(3) or outer proton with coordinate ($x$, 0, $z$) is located on a mirror site, it points towards the interlayer, while the H(4) or inner proton is located on a three-fold rotational axis with coordinate (0, 0, $z$); it points inside the di-trigonal rings formed by the tertahedra, and has a structural environment very similar to that of the protons in talc (Stixrude, 2002). There are four distinct oxygen atom environments, the O(1) atoms correspond to the apical positions of the $SiO_4$ tetrahedra, O(2) atoms form the basal plane of the tetrahedral rings, O(4) and O(3) atom are associated with Mg–O octahedral layer and are both attached to protons (Fig. 2, supplementary Table).

As the structure is compressed, the tetrahedral units and octahedral units behave differently reflecting the constrast in bond strength. Mg–O octahedral units are relatively compressible with a polyhedral bulk modulus $K_{oct}=132$ GPa. The bulk modulus of the $MgO_6$ polyhedra are similar to talc (140 GPa, Stixrude, 2002) and other silicates (150 GPa, Hazen and Finger, 1979). The linear bulk modulus along $a$-axis is softer than the Mg-octahedral bulk modulus ($K_{oct}=132$ GPa$>K_a/3=127$ GPa) indicating that Mg-octahedra are not compressed isotropically. At low pressure Mg-octahedra are flattened ($\psi=60°$ at ambient pressure) in the

**Table 1**
Equation of state parameters for high and low-pressure phases of serpentine from theory and experimental study

| $V_o$ (Å$^3$) | $K_o$ (GPa) | $K_0'$ | $K_0''$ | Reference |
|---|---|---|---|---|
| *This study* | | | | |
| GGA (static) | | | | |
| 186.34 | 41.36 | 12.38 | −2.05 | lo-P |
| 203.15 | 35.64 | 4.09 | | int-P |
| 170.51 | 82.62 | 4.14 | | hi-P |
| LDA (static) | | | | |
| 170.76 | 79.93 | 12.34 | −2.56 | lo-P |
| 173.52 | 74.61 | 3.10 | | int-P |
| 158.88 | 95.78 | 4.19 | | Hi-P |
| LDA (300 K) | | | | |
| 174.02 | 61.05 | 17.25 | −5.62 | lo-P |
| *Experimental methods* | | | | |
| 172.00 | 62.03 | 6.39 | | SXRD[a] |
| 178.40 | 57.00 | | | SCXRD[b] |
| 184.06 | 63.50 | 2.77 | | *Shock Wave*[c] |

[a] SXRD: synchroton X-ray diffraction (Hilairet et al., 2006b).
[b] SCXRD: single crystal X-ray diffraction (Mellini and Zanazzi, 1989).
[c] SW: Shock wave method, low pressure phase (Tyburczy et al., 1991).

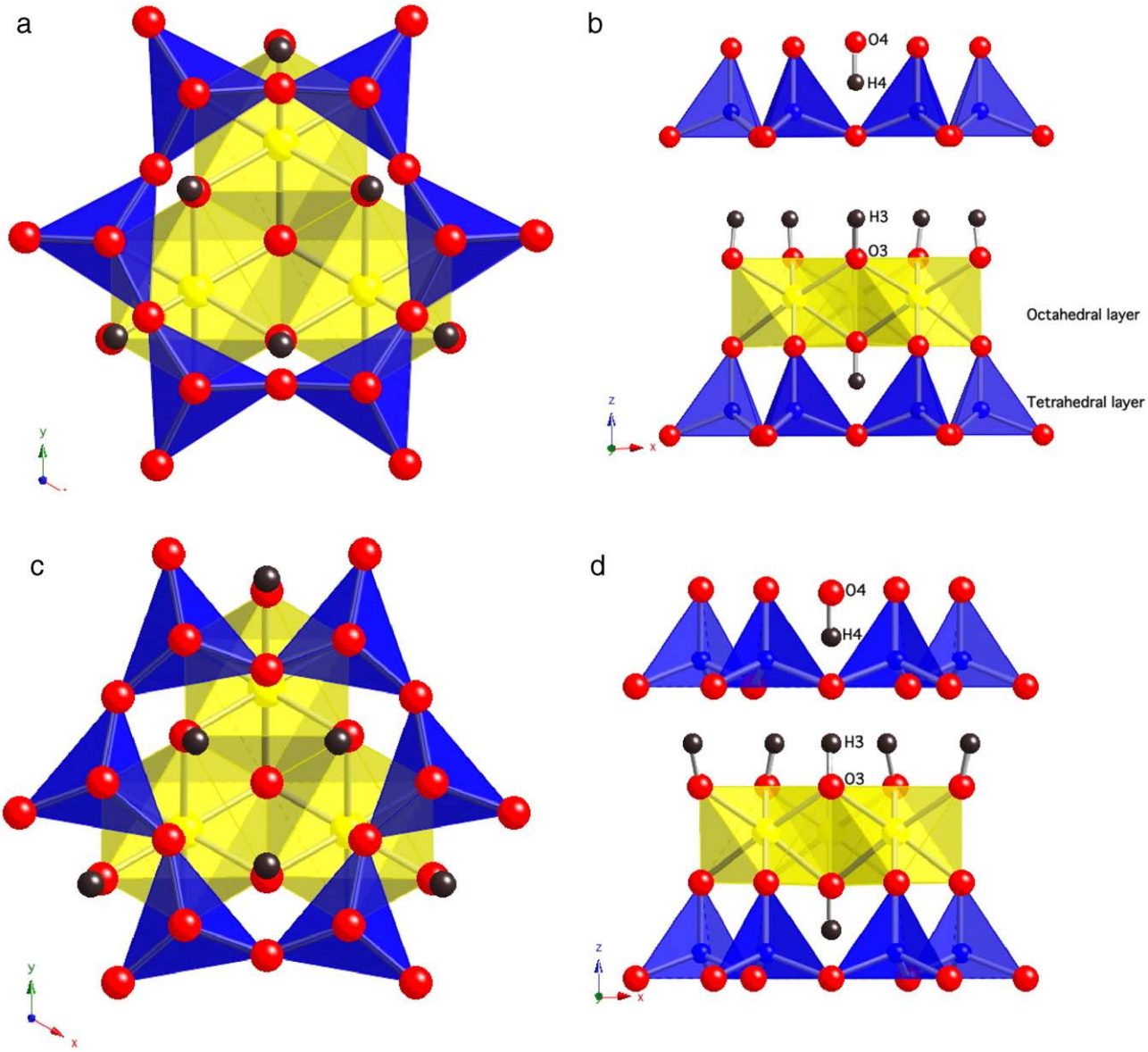


**Fig. 2.** Predicted structure of serpentine at a) $V=180$ Å$^3$ and b) $V=135$ Å$^3$ viewed down [001] direction. The $SiO_4$ tetrahedra (blue) form hexagonal ring and di-trigonal ring at $V=180$ Å$^3$ and $V=135$ Å$^3$ respectively. The protons (black spheres) point outward and inward at $V=180$ Å$^3$ and $V=135$ Å$^3$ respectively.

[001] direction and become more ideal upon compression ($\psi=55^\circ$ at ~180 GPa, the ideal value being $\psi=\cos^{-1}\left(1/\sqrt{3}\right)\approx 54.7^\circ$). For such reduction in flattening, the octahedral must compress more in [100] direction than in [001] direction explaining the difference between $K_{oct}$ and $K_a$. The octahedral quadratic elongation ($\langle\lambda_{oct}\rangle=\sum_{i=1}^{6}(l_i/l_o)^2/6$ (Robinson et al., 1971) where $l_o$ is the center to vertex distance for a regular octahedron whose volume is equal to the distorted octahedron with bond lengths $l_i$) shows discontinuities in pressure-dependence at 7 and 22 GPa indicating changes in mode of deformation of the octahedra. Keeping registry with the octahedral units, tetrahedral rings display similar discontinuities in terms of tetrahedral rotation angle, the average tetrahedral bond length and the tetrahedral volume. The tetrahedral compressibility is 187 GPa (for unit-cell volume greater than 160 Å$^3$), and 656 GPa (for unit-cell volume less than 140 Å$^3$) for the low and high pressure regime (Fig. 3a). In the intermediate region (for unit-cell volume in between 160 Å$^3$ and 140 Å$^3$) the tetrahedral volume increases slightly with pressure so that the tetrahedral bulk modulus vanishes and becomes negative in this region. We attribute the unusual negative value of the tetrahedral bulk modulus to interactions with the O(3)–H(3) hydroxyl, as the O(3)–H(3) hydroxyl flips to interact with a new set of basal oxygens. Interactions with the hydroxyl also cause the Si–O–Si angle to decrease most rapidly in the intermediate pressure regime (Fig. 3b).

The position and orientation of the inner hydroxyl O(3)–H(3) is characterized by the angle θ between the hydroxyl vector O(3)–H(3) and [001] direction. If the O(3)–H(3) vector is tilted away from the center of the di-trigonal ring formed by $SiO_4$ tetrahedra, $\theta$ is defined as negative, whereas, if O(3)–H(3) is tilted towards the center, it is defined as positive. In this study, we find that at ambient conditions, the O(3)–H(3) hydroxyl points outwardly from the center of the di-trigonal rings formed by the tetrahedral units i.e., $\theta$ is positive (Fig. 4a). In association with the distortion of the tetrahedral rings upon compression, the orientation of the hydroxyl gradually evolves. Upon compression the hydroxyl vector becomes vertical and finally tilts inwards, while always remaining on the ($x$, 0, $z$) mirror plane. Pressure-induced proton reorientation has been reported in other layered hydrous silicates such as dickite (Johnston et al., 2002). In

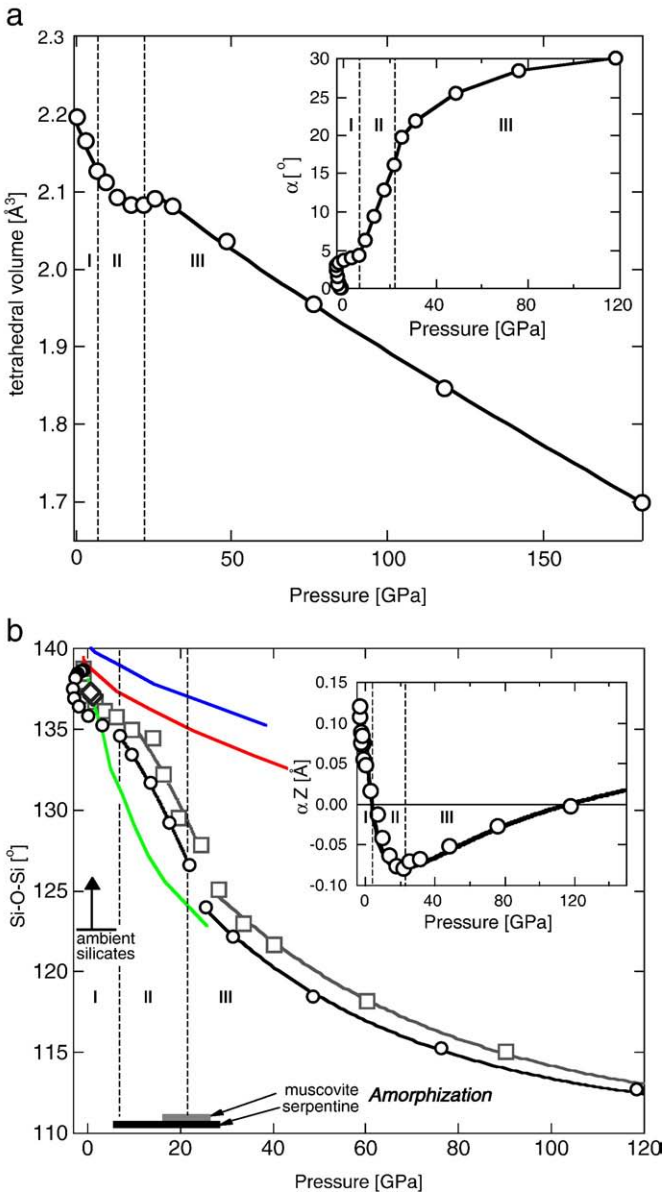


**Fig. 3.** a) Variation of tetrahedral volume ($V_{SiO_2}$) with pressure shows distinct discontinuity at 22 GPa and a subtle discontinuity at 7 GPa, inset shows evolution of the tetrahedral angle ($\alpha$) with compression; b) Theoretical prediction of Si–O–Si angles in serpentine, open circle, LDA; open square, GGA; solid line, fit to the variation of Si–O–Si angle; red and blue solid lines, 10 Å phase with 1 and 2 water molecule respectively, (Fumagalli and Stixrude, 2007), green solid line, talc (Stixrude, 2002). Si–O–Si values observed at ambient conditions (horizontal line and arrow, O'Keeffe and Hyde, 1978), range of pressure over which serpentine (Meade and Jeanloz, 1991) and muscovite (Faust and Knittle, 1994) are observed to become amorphous. Inset shows the misfit between octahedral layer and tetrahedral layer, denoted by $\Delta z=[zO_{max}-zO_{min}]\times c$, shows null value and minimum as the structure undergoes transformations at 7 and 22 GPa respectively.

tandem with the reorientation of the proton, the hydrogen bond angle O–H…O also exhibits discontinuities at 7 and 22 GPa corresponding to the structural reorganization of the framework (Fig. 4a).

We find that serpentine shows little evidence of hydrogen bonding (Fig. 4b). At low pressures corresponding to volumes greater than the theoretically determined zero pressure volume, $r_{OH}$ increases slightly on compression up to 0.4 GPa and eventually decreases upon further compression. This behavior is opposite to that expected of hydrogen bonds in which, as the O–O distance (rOO) decreases, the O–H distance (rOH) increases towards rOO/2 (symmetric hydrogen bonding), accompanied by a strengthening of the hydrogen bond and a decrease in the OH stretching frequency. In serpentine, the absence of normal hydrogen bond behavior on compression is influenced by the non-linear geometry of the bond, and by the flip in the orientation of the hydroxyl (Fig. 4a). Our results are consistent with experimental measurements of the high-pressure Raman spectrum of serpentine (Auzende et al., 2004), which show that the stretching modes of the outer hydroxyl increases with increasing pressure at a rate $\partial\nu/\partial P=+7$–11 $cm^{-1}$/GPa for a variety of serpentine polytypes. Mizukami et al. (2007) also finds a positive pressure derivative, although with a lower magnitude $\partial\nu/\partial P\sim 1.7$ $cm^{-1}$/GPa. Atomistic energy simulations of

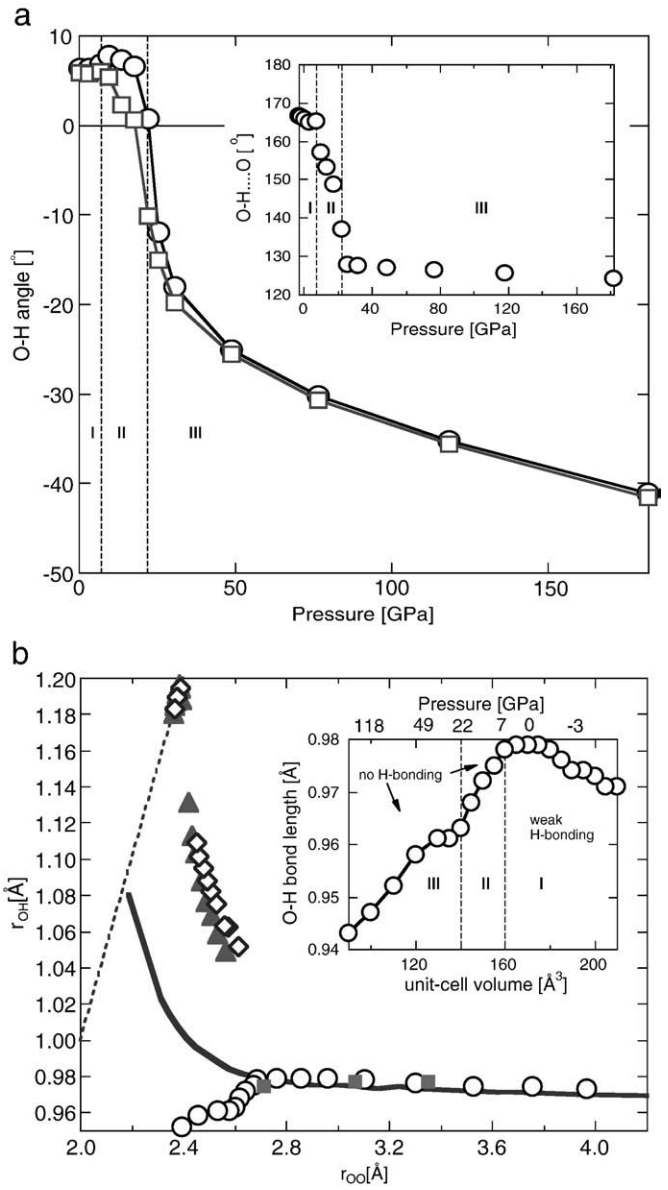


**Fig. 4.** a) Theoretical prediction of angle between hydroxyl (O–H) vector and [001] direction in serpentine, black open circle and line, LDA; grey open square and line, GGA; the dashed lines separates the three regions based on discontinuity in equation of state. Inset shows the behavior of the O–H…O angle, note the discontinuity at 7 and 22 GPa; b) Plot of $r_{OH}$ as a function of $r_{OO}$, the dashed line depicts the condition for symmetric hydrogen bonding i.e., $r_{OO}=2r_{OH}$. The black open circles refers to LDA results for serpentine, solid lines are for brucite (Mookherjee and Stixrude, 2006) grey filled squares are for talc (Stixrude, 2002), black open rhombs and filled grey triangles phase D and δ-AlOOH (Tsuchiya et al., 2005; Panero and Stixrude, 2004). Inset shows the LDA results for O(3)–H(3) hydroxyl (open circle) bond length increase at large volumes corresponding to pressures of around 7 GPa, after which the O(3)–H(3) hydroxyl bond length decreases indicating non-hydrogen bond state. Note a distinct kink in pressure dependence of O(3)–H(3) at around 22 GPa.

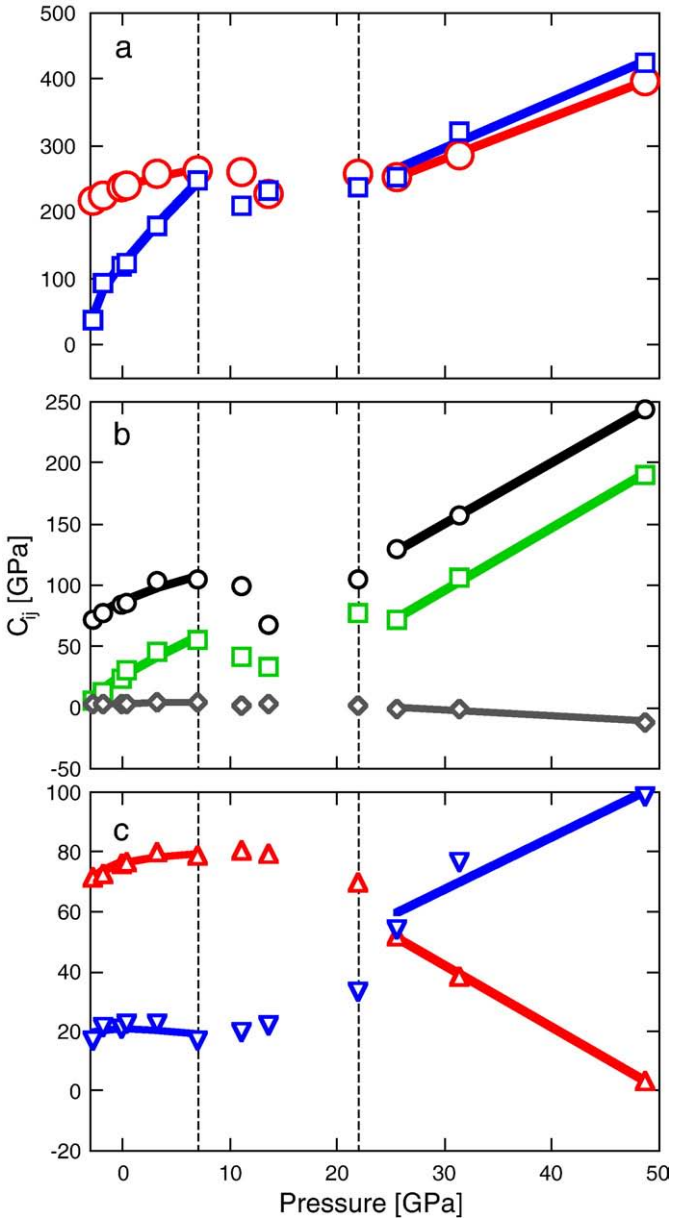


**Fig. 5.** Elastic constants vs. pressure: the symbols are from LDA theory, a) red open circle, $c_{11}$; blue open square, $c_{33}$; b) black circle $c_{12}$; green square, $c_{13}$; grey rhombs, $c_{14}$; c) blue downward triangle, $c_{44}$; red upward triangle, $c_{66}$. Bold line represents finite strain fit to the theory.

serpentine, also predict weak hydrogen bonding at ambient conditions (Benco and Smrock, 1998; Balan et al., 2002). The value of $\partial\nu/\partial P$ for the inner hydroxyl in serpentine is very similar to that found in talc (1.1–2.1 $cm^{-1}$/GPa) (Holtz et al., 1993; Scott et al., 2007), as expected based on the similar structural environments.

We predict a break in slope of the frequency of the outer hydroxyl stretch with increasing pressure associated with the proton reorientation (7 GPa at static conditions). At room temperature, the transition from low- to intermediate-pressure regimes should occur at slightly higher pressure, which may be why a break in slope was not seen in the experiments of Auzende et al. (2004) up to 10 GPa. Our prediction is consonant with results on structurally related materials. For example, in clinochlore, the outer hydroxyl stretching frequency exhibits distinct breaks in $\partial\nu/\partial P$ at around 9 GPa indicating a transition from weak to non-hydrogen bonded state (Kleppe et al., 2003). The proton reorientation in dickite is associated with a change in the pressure derivative of the hydroxyl stretching frequency $\partial\nu/\partial P$ from −6.3 to +7.2 $cm^{-1}$/GPa, also indicating a change in hydrogen bonding (Johnston et al., 2002).

### 3.3. Elasticity

Because single crystals of sufficient size are difficult to synthesize, very few experimental data on elasticity of clays exist (Vaughan and Guggenheim, 1986). Serpentine crystallizes in the trigonal system (Laue class $\bar{3}m$), which is characterized by six independent elastic stiffness constants $c_{11}$, $c_{33}$, $c_{44}$, $c_{12}$, $c_{13}$ and $c_{14}$, with $c_{66}=(c_{11}-c_{12})/2$, and $c_{56}=-c_{24}=c_{14}$ (Nye, 1985) (Fig. 5).

The calculated elastic constants may be compared with those of other layered structures, which also show substantially softer elastic response in the stacking direction (Table 2). The elastic constants exhibit striking anisotropy at ambient pressures. At ambient pressures, $c_{11}$ is 2.4 times greater than $c_{33}$, reflecting weaker bonding along [001] direction. This is in accordance with the observed pressure dependence of $c/a$. Upon compression $c_{33}$ increases more rapidly than $c_{11}$ and at 7 GPa they are almost equal. The strong anisotropy is also reflected in shear via the ratio ($c_{66}/c_{44}$), where $c_{66}$ governs shear deformation of the T–O sheets, and $c_{44}$ shear sliding of sheets across each other, which decreases from 3.67 at ambient conditions to 1.3 at 22 GPa. The elastic constants of serpentine increase monotonically with pressure until ~7 GPa. Between 7 GPa and 22 GPa, several elastic constants soften and at pressures greater than 22 GPa, the shear anisotropy ($c_{66}/c_{44}$) inverts and the structure becomes stiffer with increasing pressure. At pressures greater than 50 GPa, $c_{66}$ becomes negative indicating a mechanical instability (Nye, 1985).

Isotropically averaged bulk and shear moduli, and the compressional and shear wave velocities are in good agreement with our computed equation of state, and with experimental measurements (Table 2). In order to compare with room temperature experimental data, we apply the Debye–Mie–Grüneisen model with parameter values as discussed above, in addition to the shear part of the strain-derivative of the Grüneisen parameter $\eta_S=1.36$ as determined from our computed value of $G$ and systematic relations (Stixrude and Lithgow-Bertelloni, 2005). We find values at zero pressure and 300 K of the adiabatic bulk modulus $K_S=61$ GPa, shear modulus $G=35$ GPa, and P- and S-wave velocities $V_P=6.36$ km $s^{-1}$, $V_S=3.63$ km $s^{-1}$, as

**Table 2**
Elastic constants ($c_{ij}$), bulk ($K_0$) and shear ($G_0$) modulus of hydrous silicate phases

| (GPa) | Serpentine | | Phase D[1] | Brucite[2] | Muscovite[3] | Talc[4a] | Talc[4b] |
|---|---|---|---|---|---|---|---|
| | $M_O$ | M' | $M_O$ | $M_O$ | $M_O$ | $M_O$ | $M_O$ |
| $c_{11}$ | 235.61 | 6.16 | 387.7 | 154 | 181 | 219.83 | 243.23 |
| $c_{33}$ | 118.16 | 23.91 | 287.7 | 49.7 | 58.6 | 48.89 | 53.72 |
| $c_{44}$ | 20.92 | 0.88 | 100.4 | 21.3 | 16.5 | 26.54 | 40.12 |
| $c_{12}$ | 85.96 | 5.12 | 108.0 | 42.1 | 48.8 | 59.66 | 96.35 |
| $c_{13}$ | 25.05 | 7.00 | 51.1 | 7.8 | 25.6 | −4.82 | 23.56 |
| $c_{14}$ | 2.69 | 0.26 | −14.6 | 1.3 | | −0.82 | |
| Bulk Modulus | | | | | | | |
| Voigt | 95.66 | 5.49 | | | | | |
| Hill | 88.18 | 7.09 | 161.64 | 43.8 | 58.2 | 42.08 | 64.99 |
| Reuss | 80.69 | 9.00 | | | | | |
| Shear Modulus | | | | | | | |
| Voigt | 53.85 | 0.91 | | | | | |
| Hill | 45.04 | 0.78 | 122.03 | 35.2 | 35.3 | 40.44 | 54.60 |
| Reuss | 36.23 | 0.59 | | | | | |

1(Mainprice et al., 2007), 2(Jiang et al., 2006), 3(Vaughan and Guggenheim, 1986): the remaining elastic constants for muscovite are $c_{22}=178.4$, $c_{55}=19.5$, $c_{23}=21.2$, $c_{15}=-14.2$, $c_{25}=1.1$, $c_{35}=1.0$, $c_{46}=-5.2$ GPa, 4a ($C\bar{1}$) and 4b ($C2/c$) respectively (Mainprice et al., 2008); the remaining elastic constant for talc ($C\bar{1}$) are $c_{15}=-33.87$, $c_{16}=-1.04$, $c_{22}=216.38$, $c_{23}=-3.67$, $c_{24}=1.79$, $c_{25}=-16.51$, $c_{26}=-0.62$, $c_{34}=4.12$, $c_{35}=-15.52$, $c_{36}=-3.59$, $c_{45}=-3.60$, $c_{46}=-6.41$, $c_{55}=22.85$, $c_{56}=-1.67$, $c_{66}=78.29$ and for talc ($C2/c$) are $c_{15}=-29.94$, $c_{22}=256.62$, $c_{23}=10.25$, $c_{25}=-15.24$, $c_{35}=-19.05$, $c_{46}=-5.48$, $c_{55}=54.92$, $c_{66}=74.49$ GPa.

compared with experimental values for antigorite: $K_S$=69 GPa, and $G$=34 GPa, $V_P$=6.52 km s$^{-1}$, $V_S$=3.57 km s$^{-1}$ (Christensen, 2004). The difference between theoretical and experimental values of $K_S$ and $V_P$ may be due to the difference in polytypes: indeed, antigorite is found experimentally to be slightly denser than lizardite, and so is expected to have a larger bulk modulus.

## 4. Discussion and conclusion

We find three distinct regimes of compression in lizardite, distinguished by structural features and compression mechanisms:

1) low pressure ($P$<7 GPa) The hydroxyl points outward from the centers of the ditrigonal rings, weak hydrogen bonding is present, and the elastic constants increase monotonically on compression.
2) intermediate pressure (7<$P$<22 GPa) The hydroxyl rapidly moves towards the vertical, causing the Si–O–Si angle to decrease rapidly, and tetrahedra to expand on compression. Several elastic constants decrease with increasing pressure. Compression becomes nearly isotropic as the c/a ratio changes little with pressure.
3) High pressure ($P$>22 GPa). The hydroxyl points inward, the longitudinal elastic constants increase on compression, and mechanical instability sets in via vanishing of $c_{66}$ near 50 GPa.

The unusual compressional behavior of serpentine may shed light on the origin of its pressure-induced amorphization. Pressure-induced amorphization of serpentine has been suggested as a source of intermediate depth earthquakes (Meade and Jeanloz, 1991) although subsequent experiments find that amorphization occurs only at temperatures that are lower than those expected in the top of the subducting slab (Irifune et al., 1996). Amorphization is found to occur over a pressure interval very similar to our intermediate pressure regime. Indeed, the unusual structural and compressional features of the intermediate pressure regime result from a mismatch of structural features (T and O sheets, and rearrangement of hydrogen bonds) that tend to make the structure unstable, which may be the cause of amorphization.

The intermediate pressure regime also includes the kinetically hindered extension to room temperature of the high pressure dehydration of serpentine to a denser $H_2O$-bearing assemblage. Amorphization and dehydration may be genetically linked. Pressure-induced amorphization has been associated with crossing of the metastable extensions of reactions or kinetically hindered reactions with negative Clapeyron slopes ($dP/dT=\Delta S/\Delta V$) (Hemley et al., 1988). Dehydration reactions of hydrous phases typically have a positive and shallow Clapeyron slope at low pressure, and a negative slope at higher pressure as the fluid compresses much more rapidly than the solid phases, reversing the sign of $\Delta V$. Indeed, the pressure of room temperature amorphization corresponds closely to the kinetically hindered extension of the dehydration reaction curve in serpentine.

The bulk modulus of layered hydrous silicates exhibits a strong correlation with the linear moduli along the [001] direction, indicating that at low-pressures the compression of the structure is primarily controlled by the compression along the [001] direction (Fig. 1b). Most of the hydrous phases undergo substantial compression along [001] direction accompanied by an initially rapid decrease of $c/a$ with increasing pressure and then flattening out as the [001] direction is compressed. This is also manifested by the behaviour of the $c_{11}$ and $c_{33}$ elastic constants with pressure.

The structure of serpentine exhibits striking anisotropy at low pressure conditions, azimuthal anisotropy of P-waves ($A_P$) (Karki et al., 2001) is around 41% at ambient pressures, the anisotropy however reduces to around 25% at 7 GPa, then shows a small increment and further reduction to 19% at 22 GPa. Corresponding values for S-waves ($A_S$) varies from 62% at 0 GPa to 50% at 22 GPa. Remarkably, samples of natural serpentinite that have been studied to date show little bulk anisotropy, indicating nearly random orientations of crystallites in the

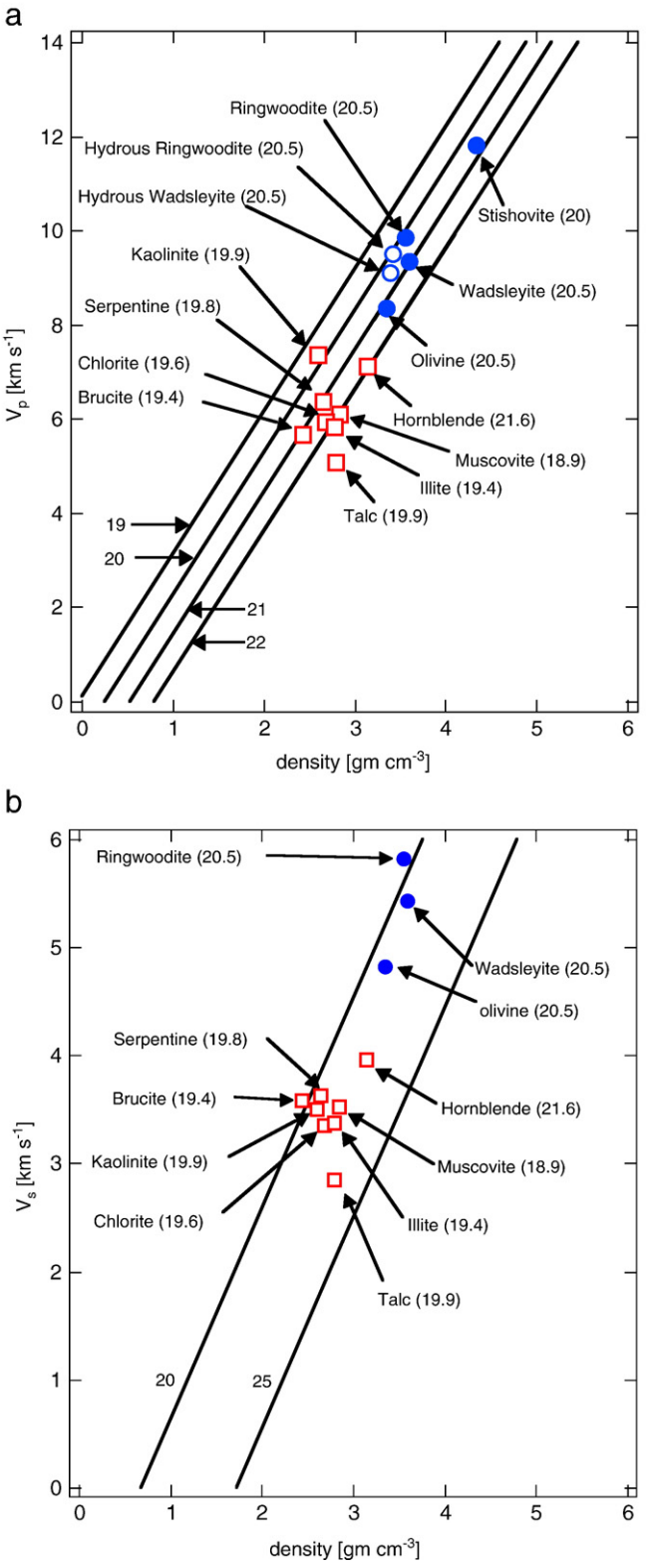


**Fig. 6.** Velocity density systematics, a) compressional wave and b) shear wave, the lines corresponds to the mean atomic weights, the data for major mantle phases from Stixrude and Lithgow-Bertelloni 2005. Note that the mean atomic weight for hydrous silicates are estimated with OH taken as a single atom. Hydrous silicates are compiled from literature, serpentine, present study; talc, Bailey and Holloway (2000); muscovite, Vaughan and Guggenheim (1986); hornblende, Bass (1999); brucite, Jiang et al. (2006); kaolinite, Sato et al. (2005); illite and chlorite, Katahara (1996); hydrous wadsleyite, Mao et al. (2008); hydrous ringwoodite, Inoue et al. (1998), wadsleyite, ringwoodite, olivine are from Stixrude and Lithgow-Bertelloni, 2005 and references there in.

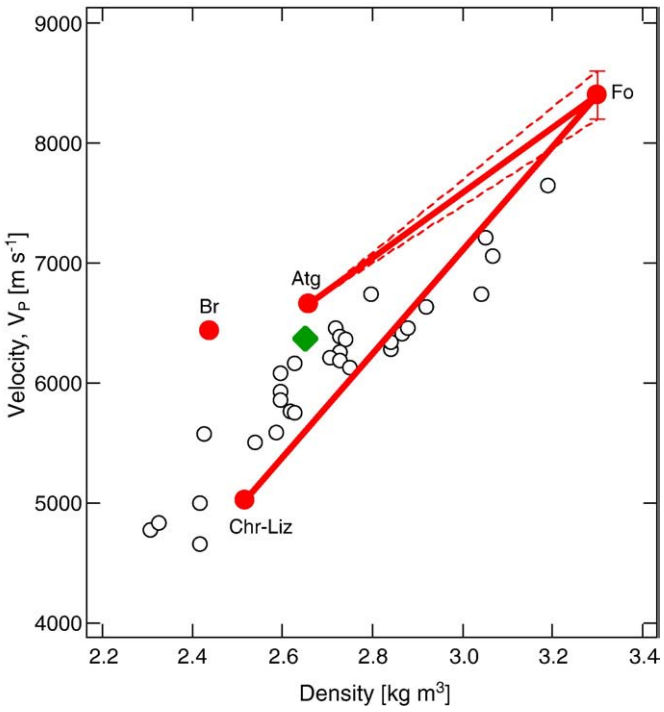


**Fig. 7.** Comparison of compressional wave velocities plotted against density (rock or mineral); filled circles (red) are acoustic measurements from Christensen (2004) fior peridotites dominated by olivine component (Fo), brucite (Br), chrysotile–lizardite (Chr-Liz) and antigorite (Atg); open circles are partially or totally serpentinized peridotites (from Christensen, 2004); green rhomb, present study. Strong reduction in partially or totally serpentinized peridotites are probably due to contribution from chrystotile, which often forms nanotubes which accounts for large porosities and reduction of seismic wave velocities (Reynard et al., 2007).

poly-crystalline rock (Christensen, 2004). Further experimental studies and in situ seismological observations will be needed to determine whether preferred orientation, and therefore whole rock anisotropy can develop in serpentinites in some geodynamic settings.

The concept of velocity density systematics has been extremely important in geophysics (Birch, 1960). Birch's law

$$V_p = a(\overline{m}) + b\rho \tag{3}$$

relates compressional velocity ($V_p$) to density ($\rho$) of a mineral for a given mean atomic weight ($\overline{m}$). The relationship holds whether density is varied by compression or by phase transformation and has been used to construct velocity-density profiles of earth as silicate minerals undergo phase transformations, where the traditional Adams–Williamson approach fails. Birch's law is empirical. Recent experiments have questioned its validity at high temperatures in the case of iron (Lin et al., 2005). Major mantle minerals do tend to obey Birch's law (Karki et al., 2001; Stixrude and Lithgow-Bertelloni, 2005): for similar mean atomic weights, denser minerals are faster.

We use Birch's law to ask a simple question: are hydrous phases slower than anhydrous phases of otherwise similar composition primarily because the hydrous phases are less dense, or because of some property unique to the hydrogen bond. We find that hydrous minerals tend to obey Birch's law approximately as well as anhydrous minerals (Fig. 6). In making this comparison, we have computed the mean atomic weight for the hydrous phases taking OH units as single atoms. Such assumption is justified since hydrogen is attached to adjacent oxygen atoms, thus limiting its repulsive potential in the structure (Smyth and Jacobsen, 2007). This comparison shows that hydrous phases are slower primarily because they are less dense.

The S-wave and P-wave velocities obtained in our study, while similar to those of antigorite serpentinites are significantly higher than those of lizardite–chrysotile bearing serpentinites measured experimentally (Christensen, 1966). The differences are very large: 2 km/s or 100% in $V_S$ and 2 km/s or 40% in $V_P$ (Fig. 7).

Comparison of our calculated elastic wave velocities to measured velocites of serpentinites indicates: 1) that lizardite and antigorite have similar elastic wave velocities and 2) that chrysotile is much slower, possibly due to its tubular crystal-habit. Our computed P- and S-wave velocities of lizardite are much closer to those of antigorite-bearing serpentinites (Christensen, 1978) than to those of chrysotile–lizardite-bearing serpentinites (Christensen, 1966). These comparisons indicate that it is the chrysotile, rather than the lizardite, component of the chrysotile–lizardite–serpentinites that causes the anomalously low velocities in these samples and that lizardite is a good elastic analog of antigorite. Another recent study (Reynard et al., 2007) came to similar conclusions.

Previous analyses of the hydration of the mantle wedge based on comparisons of seismic observations to the properties of chrysotile–serpentines, are likely erroneous (Bostock et al., 2002; Carlson and Miller, 2003; Hyndman and Peacock, 2003). It is antigorite, not chrysotile, that is the stable polytype in the mantle wedge. Because antigorite is much faster, the amount of hydration inferred from mantle seismic velocites is much greater than previously thought. Indeed, mantle wedge seismic velocities are comparable to, or ever slower than those of pure antigorite-serpentinite. It thus seems likely that other phases contribute to the anomalously low seismic wave velocities and inverted mohos seen in some mantle wedges, such as brucite, talc, or even free fluid/melt.

## Acknowledgement

This work was supported by US National Science Foundation grant to LPS. The comments of Prof. David Mainprice and an anonymous reviewer are gratefully acknowledged.

## Appendix A. Supplementary data

Supplementary data associated with this article can be found, in the online version, at doi:10.1016/j.epsl.2008.12.018.

## References

Auzende, A.-L., Daniel, I., Reynard, B., Lemaire, C., Guyot, F., 2004. High-pressure behaviour of serpentine minerals: a Raman spectroscopic study. Phys. Chem. Mineral. 31, 269–277.
Auzende, A.-L., Pellenq, R.J.-M., Devouard, B., Baronnet, A., Grauby, O., 2006. Atomistic calculations of structural and elastic properties of serpentine minerals: the case of lizardite. Phys. Chem. Mineral. 33, 266–275.
Bailey, E., Holloway, J.R., 2000. Experimental determination of elastic properties of talc to 800 °C, 0.5 GPa; calculations of the effect of hydrated peridotite and implications for cold subduction zones. Earth Planet. Sci. Lett. 183, 487–498.
Balan, E., Saitta, M.A., Mauri, F., Lemaire, C., Guyot, F., 2002. First-principle calculation of the infrared spectrum of lizardite. Am. Mineral. 87, 1286–1290.
Bass, J.D., 1999. Elasticity of minerals, glasses and melts. Mineral Physics and Crystallography Handbook of physical constants. American Geophysical Union. reference shelf 2.
Benco, L., Smrock, L., 1998. Hartree–Fock study of pressure-induced strengthening of hydrogen bonding in lizardite-1T. Eur. J. Mineral. 10, 483–490.
Birch, F., 1960. The velocity of compressional waves in rocks to 10-kilobars.1. J. Geophys. Res. 65, 1083–1102.
Birch, F., 1978. Finite strain isotherm and velocities for single-crystal and polycrystalline NaCl at high-pressure and 300 K. J. Geophys. Res. 83, 1257–1268.
Bostock, M.G., Hyndman, R.D., Rondenay, S., Peacock, S.M., 2002. An inverted continental Moho and serpentinization of the forearc mantle. Nature 417, 536–538.
Carlson, R.L., Miller, D.J., 2003. Mantle wedge water contents estimated from seismic velocities in partially serpentinized peridotites. Geophys. Res. Lett. 30, 1250. doi:10.1029/2002GL016600.
Christensen, N.I., 1966. Elasticity of ultrabasic rocks. J. Geophys. Res. 71, 5921–5931.
Christensen, N.I., 1978. Ophiolites, seismic velocities and oceanic crustal structure. Tectonophysics, 47, 131–157.
Christensen, N.I., 2004. Serpentinites, peridotites, and seismology. Int. Geol. Rev 46, 795–816.
Ciesla, F.J., Lauretta, D.S., Cohen, B.A., Hood, L.L., 2003. A nebular origin for chondritic fine-grained phyllosilicates. Science 299, 549–552.

Comodi, P., Zanazzi, P.F., 1995. High-pressure structural study of muscovite. Phys. Chem. Mineral. 22, 170–177.
Comodi, P., Zanazzi, P.F., Weiss, Z., Reider, M., Drabek, M., 1999. Cs-tetra-ferri-anite: High pressure and high-temperature behavior of a potential nuclear waste disposal phase. Am. Mineral. 84, 325–332.
Comodi, P., Cera, F., Dubrovinsky, L., Nazzareni, S., 2006. The high pressure behaviour of the 10 Å phase: a spectroscopic and diffractometric study up to 42 GPa. Earth Planet. Sci. Lett. 246, 444–457.
Dobson, D.P., Meredith, P.G., Boon, S.A., 2002. Simulation of subduction zone seismicity by dehydration of serpentine. Science 298, 1407–1410.
Faust, J., Knittle, E., 1994. The equation of state, amorphization, and high-pressure phase — diagram of muscovite. J. Geophys. Res. 99, 19785–19792.
Frost, D.J., Fei, Y., 1999. Static compression of the hydrous magnesium silicate phase D to 30 GPa at room temperature. Phys. Chem. Minerals. 26, 415–418.
Fumagalli, P., Stixrude, L., 2007. The 10 Å phase at high pressure by first principles calculations and implications for the petrology of subduction zones. Earth Planet. Sci. Lett. 260, 212–226.
Fryer, P., Wheat, C.G., Mottl, M.J., 1999. Mariana blueschist mud volcanism: Implications for conditions within subduction zone. Geology 27, 103–106.
Gregorkiewitz, M., Lebech, B., Mellini, M., Viti, C., 1996. Hydrogen positions and thermal expansion in lizardite-1T from Elba: a low-temperature study using Rietveld refinement of neutron diffraction data. Am. Mineral. 81, 1111–1116.
Grobéty, G., 2003. Polytypes and higher-order structures of antigorite: A TEM study. Am. Mineral. 88, 27–36.
Hazen, R.M., Finger, L.W., 1978. The crystal structures and compressibilities of layer minerals at high pressure. II Phlogopite and chlorite. Am. Mineral. 63, 293–296.
Hazen, R.M., Finger, L.W., 1979. Bulk modulus–volume relationship for cation–anion polyhedra. J. Geophys. Res. 84, 6723–6728.
Heine, V., 1970. The pseudopotential concept. Solid State Phys. 24, 1–37.
Hemley, R.J., Jephcoat, A.P., Mao, H.K., Ming, L.C., Manghnani, M.H., 1988. Pressure-induced amorphization of crystalline silica. Nature 334, 52–54.
Hilairet, N., Daniel, I., Reynard, B., 2006a. Equation of state of antigorite, stability field of serpentines, and seismicity in subduction zone. Geophys. Res. Lett. 33 L023021-4.
Hilairet, N., Daniel, I., Reynard, B., 2006b. P–V equation of state and relative stabilities of serpentine varieties. Phy. Chem. Min. 33, 629–637.
Hilairet, N., Reynard, B., Wang, Y., Daniel, I., Merkel, S., Nishiyama, N., Petitgirard, S., 2007. High-pressure creep of serpentine, interseismic deformation, and initiation of subduction. Science 318, 1910–1913.
Holtz, M., Solin, S.A., Pinnavaia, T.J., 1993. Effect of pressure on Raman vibrational modes of layered aluminosilicate compounds. Phys. Rev. B 48, 13312–13317.
Hyndman, R.D., Peacock, S.M., 2003. Serpentinization of the forearc mantle, Earth Planet. Sci. Lett. 212, 417–432.
Inoue, T., Weidner, D.J., Northrup, P.A., Parise, J.B., 1998. Elastic properties of hydrous ringwoodite (γ-phase) in $Mg_2SiO_4$. Earth Planet. Sci. Lett. 160, 107–113.
Irifune, T., Kuroda, K., Funamori, N., Uchida, T., Yagi, T., Inoue, T., Miyajima, N., 1996. Amorphization of serpentine at high pressure and high temperature. Science 272, 1468–1470.
Jiang, F., Speziale, S., Duffy, T., 2006. Single-crystal elasticity of brucite, $Mg(OH)_2$ to 15 GPa by Brillouin Scattering. Am. Mineral. 91, 1893–1900.
Johnston, C.T., Bish, D.L., Dera, P., Agnew, S.F., Kenney, J.W., 2002. Novel pressure-induced phase transformations in hydrous layered materials. Geophys. Res. Lett 29, GL015402,17-1-17-4.
Karki, B.B., Stixrude, L., Wentzcovitch, R.M., 2001. High-pressure elastic properties of major materials of earth's mantle from first principles. Rev. Geophys. 39, 507–534.
Katahara, K.W., 1996. Clay mineral elastic properties. SEG Ext. Abstr. 15, 1691–1694. doi:10.1190/1.1826454.
Kleppe, A.K., Jephcoat, A.P., Welch, M.D., 2003. The effect of pressure upon hydrogen bonding in chlorite: A Raman spectroscopic study of clinochore to 26.5 GPa. Am. Mineral. 88, 567–573.
Kohn, W., Sham, L.J., 1965. Self-consistent equations including exchange and correlation effects. Phys. Rev. A 140, 1133–1138.
Kresse, G., Furthmüller, J., 1996a. Efficiency of ab-initio total energy calculations for metals and semiconductors. Comput. Mater. Sci. 6, 15–50.
Kresse, G., Furthmüller, J., 1996b. Efficient iterative schemes for ab initio total-energy calculations using plane-wave basis set. Phys. Rev. B 54, 11169–11186.
Kresse, G., Hafner, J., 1993. Ab initio molecular-dynamics for liquid metals. Phys. Rev. B 47, 558–561.
Kresse, G., Hafner, J., Needs, R.J., 1992. Optimized norm-conserving pseudopotentials. J. Phys. Condens. Matter 4, 7461–7468.
Lin, J.F., Sturhahn, W., Zhao, J.Y., Shen, G.Y., Mao, H.K., Hemley, R.J., 2005. Sound velocities of hot dense iron: Birch's law revisited. Science 308, 1892–1894.
Lundqvist, S., March, N.H., 1987. Theory of the Inhomogeneous Electron Gas. Plenum, New York.
Mainprice, D., Le Page, Y., Rodgers, J., Jouanna, P., 2007. Predicted elastic properties of hydrous D phase at mantle pressures: Implications for the anisotropy of subducted slabs near 670-km discontinuity and in the lower mantle. Earth Planet. Sci. Lett. 259, 283–296.
Mainprice, D., Le Page, Y., Rodgers, J., Jouanna, P., 2008. Ab initio elastic properties of talc from 0 to 12 GPa: Interpretation of seismic velocities at mantle pressures and prediction of auxetic behaviour at low pressure. Earth Planet. Sci. Lett. 274, 327–338.
Mao, Z., Jacobsen, S.D., Jaing, F., Symth, J.R., Holl, C.M., Frost, D.J., Duffy, T.S., 2008. Single-crystal elasticity of wadsleyite, β-$Mg_2SiO_4$, containing 0.37–1.66 wt. $H_2O$. Earth Planet. Sci. Lett. 266, 78–89.
Meade, C., Jeanloz, R., 1990. Static compression of $Ca(OH)_2$ at room temperature: observation of amorphization and equation of state measurements to 10.7 GPa. Geophys. Res. Lett 17, 1157–1160.
Meade, C., Jeanloz, R., 1991. Deep-focus earthquakes and recycling of water into the Earth's mantle. Science 252, 68–71.
Mellini, M., Zanazzi, P.F., 1989. Effects of pressure on the structure of lizardite-1T. Eur. J. Mineral. 1, 13–19.
Mizukami, T., Kagi, H., Wallis, S.R., Fukura, S., 2007. Pressure-induced change in compressional behavior of the O–H bond in chrysotile: a Raman high-pressure study up to 4.5 GPa. Am. Mineral. 92, 1456–1463.
Monckhurst, H.J., Pack, J.D., 1976. Special points for brillouin-zone integrations. Phys. Rev. B 13, 5188–5192.
Mookherjee, M., Stixrude, L., 2006. High-pressure proton disorder in brucite. Am. Mineral. 91, 127–134.
Nye, J.F., 1985. Physical Properties of Crystals, 2nd edition. Clarendon, Oxford.
O' Keeffe, M., Hyde, B.G., 1978. On Si–O–Si configurations in silicates. Acta. Crystallogr. B 34, 27–32.
Obara, K., 2002. Nonvolcanic deep tremor associated with subduction in southwest Japan. Science 296, 1679–1681.
Panero, W.R., Stixrude, L.P., 2004. Hydrogen incorporation in stishovite at high pressure and symmetric hydrogen bonding in δ-AlOOH. Earth Planet. Sci. Lett. 221, 421–431.
Pawley, A.R., Clark, S.M., Chinnery, N.J., 2002. Equation of state measurements of chlorite, pyrophyllite, and talc. Am. Mineral. 87, 1172–1182.
Perdew, J.P., Bruke, K., Ernzerhof, M., 1996. Generalized gradient approximation made simple. Phys. Rev. Lett. 77, 3865–3868.
Reinen, L.A., 2000. Seismic and aseismic slip indicators in serpentine gouge. Geology 28, 135–138.
Reynard, B., Hilairet, N., Balan, E., Lazzeri, M., 2007. Elasticity of serpentines and extensive serpentinization in subduction zones. Geophys. Res. Lett. 34, L13307.
Robie, R.A., Hemmingway, B.S., 1995. Thermodynamic properties of minerals and related substances at 298.15 K and 1 bar ($10^5$ Pa) pressures and at higher temperatures. U. S. Geol. Surv. Bull. 2131.
Robinson, K., Gibbs, G.V., Ribbe, P.H., 1971. Quadratic elongation: A quantitative measure of distortion in coordination polyhdera. Science, 172, 567–570.
Rucklidge, J.C., Zussman, J., 1965. The crystal structure of the serpentine mineral, lizardite $Mg_3Si_2O_5(OH)_4$. Acta. Crystalogr. 19, 381–389.
Sato, H., Ono, K., Johnston, C.T., Yamagishi, A., 2005. First principle studies on elastic constants of 1:1 layered kaolinite mineral. Am. Mineral. 90, 1428–1435.
Scott, H.P., Liu, Z., Hemley, R.J., Williams, Q., 2007. High-pressure infrared spectra of talc and lawsonite. Am. Mineral. 92, 1814–1820.
Smyth, J.R., Jacobsen, S.D., 2007. Birch's Law and modeling hydration in the Earth's interior. EOS Trans. AGU 88 (23) Jt. Assem. Suppl., Abstract MR44A-01.
Stixrude, L., 2002. Talc under tension and compression: Spinodal instability, elasticity, and structure. J. Geophys. Res. 107, 2327–2336.
Stixrude, L., Lithgow-Bertelloni, C., 2005. Thermodynamics of mantle minerals — I. Physical properties. Geophy. J. Int. 162, 610–632.
Stixrude, L., Peacor, D.R., 2002. First-principles study of illite–smectite and implication for clay mineral systems. Nature 420, 165–168.
Stixrude, L., Cohen, R.E., Hemley, R.J., 1998. Theory of minerals at high pressure. In: Hemley, R., Mao, H.K. (Eds.), Ultrahigh-Pressure Mineralogy. Rev. Mineral., vol. 37. Mineral. Soc. of Am., Washington, D.C., pp. 639–671.
Tsuchiya, J., Tsuchiya, T., Suneyuki, S., 2005. First-principle study of hydrogen bond symmetrization of phase D under high pressure. Am. Mineral. 90, 44–49.
Tyburczy, J.A., Duffy, T.S., Ahrens, T.J., Lange, M.A., 1991. Shock wave equation of state of serpentine to 150 GPa: implications for the occurrence of water in the Earth's lower mantle. J. Geophys. Res. 96, 18011–18027.
Vanderbilt, D., 1990. Soft self-consistent pseudopotentials in a generalized eigen-value formalism. Phys. Rev. B, 41, 7892–7895.
Vaughan, M.T., Guggenheim, S., 1986. Elasticity of muscovite and its relationship to crystal structure. J. Geophys. Res. 91 (B5), 4657–4664.
Wallace, D.C., 1972. Thermodynamics of Crystals. Dover, New York.
Wentzcovitch, R.M., 1991. Invariant molecular dynamics approach to structural phase transitions. Phys. Rev. B 44, 2358–2361.
Wentzcovitch, R.M., Martins, J.L., Price, G.D., 1993. Ab initio molecular dynamics with variable cell shape: application to $MgSiO_3$ perovskite. Phys. Rev. Lett. 70, 3947–3950.
Xia, X., Weidner, D.J., Zhao, H., 1998. Equation of state of brucite: single-crystal Brillouin spectroscopic study and polycrystalline pressure–volume–temperature measurement. Am. Mineral. 83, 68–74.